One- and two-argument equation of state parametrizations with continuous sound speed for neutron star simulations

Gaël Servignat,[1] Philip J. Davis,[2] Jérôme Novak,[1] Micaela Oertel,[1] and José A. Pons[3]
[1]*Laboratoire Univers et Théories, Observatoire de Paris, Université PSL, CNRS,*
Université Paris-Cité, 92190 Meudon, France
[2]*Université de Caen Normandie, ENSICAEN, CNRS/IN2P3, LPC Caen UMR6534, F-14000 Caen, France*
[3]*Departament de Física Aplicada, Universitat d'Alacant, Ap. Correus 99, E-03080 Alacant, Spain*

(Received 23 November 2023; accepted 26 March 2024; published 14 May 2024)

We describe two fitting schemes that aim to represent the high-density part of realistic equations of state for numerical simulations such as neutron star oscillations. The low-density part of the equation of state is represented by an arbitrary polytropic crust, and we propose a generic procedure to stitch any desired crust to the high-density fit, which is performed to ensure continuity of the internal energy, pressure, and sound speed for barotropic equations of state that describe cold neutron stars in β equilibrium. An extension of the fitting schemes to equations of state with an additional compositional argument is proposed. In particular we develop a formalism that ensures the existence of a β equilibrium at low densities. An additional feature of this low-density model is that it can be, in principle, applied to any parametrization. The performance of the fits is checked on mass, radius and tidal deformability as well as on the dynamical radial oscillation frequencies. To that end, we use a pseudospectral single neutron star evolution code based on a nonconservative form of the hydrodynamical equations. A comparison to existing parametrizations is proposed, as far as possible, and to published radial frequency values in the literature. The static and dynamic quantities are well reproduced by the fitting schemes. Our results suggest that, even though the radius is very sensitive to the choice of the crust, this choice has little influence on the oscillation frequencies of a neutron star.

DOI: 10.1103/PhysRevD.109.103022

I. INTRODUCTION

When describing relativistic stellar structure and supernova or neutron star (NS) hydrodynamics, one needs to link the thermodynamic quantities using an equation of state (EOS). The choice of the EOS is crucial, mainly because the detailed physics at very high densities (i.e., where the strong nuclear interaction is the dominant one) are poorly understood [1]. Polytropes are characterized by a high numerical precision on the computation of thermodynamic variables due to their analytical nature, allowing them to be widely used in simulations [2–8] but are however only very crude approximations for nuclear matter in the core or for the electron Fermi gas of the crust. Therefore, more realistic approaches of complex events such as a binary neutron star merger need a detailed description of the strong nuclear interaction in the core. These nuclear EOSs, the so-called realistic EOSs, often come as tables like those given in the COMPOSE database[1] [9]. Realistic EOSs are already used in binary neutron star merger [10–13], core-collapse [14–17], protoneutron star cooling [18,19], and general relativistic magnetohydrodynamic dynamo codes [20].

However, these tables may induce numerical artifacts, degrading the overall accuracy of the simulation. First, due to the nonanalytical nature of nuclear models at high densities, the precision on the thermodynamic quantities is often far from the typical machine accuracy used in computers. This may have an impact on the computation of derivatives of the EOS, like the sound speed, or those that are necessary for interpolation. Computing the sound speed with finite-differences schemes can present nonphysical spikes that may lead to code failure. Second, increasing the complexity of physical hypotheses leads to equations of state with two or three arguments, namely by considering composition and temperature effects, meaning that even with a reasonable amount of discretization points for every argument (of the order of a hundred), the tables may contain millions of entries, and the associated files would be very large. Some EOSs even depend upon more than three arguments if more particles, such as muons, are included. Moreover, computing the thermodynamic quantities at nontabulated values has to be done with interpolation, which is in itself not a trivial problem. For example, Swesty [21] has proposed a way of interpolating tables in a thermodynamically consistent manner using Hermite cubic and quintic splines. However, this technique can

---

[1] https://compose.obspm.fr.

© 2024 American Physical Society

suffer from spurious oscillations of higher-order polynomials, especially at low densities where the derivatives can be the noisiest. Representing a table analytically is a way to avoid this problem. Several analytical representations of tabulated EOSs already exist, such as piecewise polytropes [22] that were later improved [23] and generalized (hereafter referred to as GPP) [24], spectral representations [25–27], as well as the more recent parametrizations of the sound speed [28] and of the enthalpy [29].

These representations are all dedicated to cold, β-equilibrated EOSs which only depend on one thermodynamic argument, typically chosen as the baryon number density or the (pseudo)enthalpy. Although not a parametrization, [30] gives an analytical extension of cold EOSs to arbitrary proton fraction outside of β equilibrium and to finite temperatures. We here propose an analytical representation dubbed *pseudopolytrope*, both for one- and two-argument EOSs, with corresponding analytic models for low-density parts (crust), ensuring β equilibrium in the two-argument case. To benchmark our approach for one-argument EOSs, we will compare the performances of the pseudopolytrope with a second type based on the analytical approach of Potekhin *et al.* [31] and Pearson *et al.* [32] that was designed for a very precise representation of Brussels-Montreal unified EOSs. In both cases, the fits are performed in a high-density interval corresponding to homogeneous matter in the core, and the low-density part is attached in a thermodynamically consistent manner. The fits are then tested on static quantities such as the mass, radius, and tidal deformability, and on dynamic quantities, namely the radial frequencies of spherically symmetric stars, as computed with the code that has been presented in [33]. As such, the code only takes one-argument equations of state, but to take electrons into account only the evolution equation for the electron fraction has been added in the code when using two-argument EOSs, making the generalization straightforward.

We can note here an alternative approach to include out of β-equilibrium effects in hydrodynamics simulations, as done in recent works on the so-called bulk viscosity to provide effective ways to describe such fluids out of the weak β equilibrium in general relativity [34–36]. Nevertheless, in this work we follow the transport approach in which the potential absence of weak equilibrium is considered through a separate conservation equation for the electron fraction that contains source terms to take neutrino production into account. The source terms are computed thanks to the description of neutrino emission rates found in [37].

To test our fits we choose three different EOS models, covering different techniques and a relatively large range of neutron star global properties. One model is based on relativistic density functional theory (DFT), one is based on a Skyrme (nonrelativistic) density functional and one on an empirical extension of a variational microscopic model. All of them are reasonably compatible with existing constraints from nuclear experiments, theory, and astrophysics. To be specific, for the two-argument fits we consider the lowest temperature entry of the general purpose EOS models: (i) RG(SLy4) [38,39], a nucleonic nonrelativistic DFT one; (ii) the nucleonic relativistic DFT one HS(DD2) [40,41]; as well as (iii) the SRO(APR) model [42,43]. The latter is based on the APR EOS [44], which itself is partly adjusted to the variational calculation of [45], and contains a phase transition to a pion condensate at high densities. For the corresponding one-argument fits, we use the zero temperature version of the nucleonic EOS RG(SLy4) [38,46,47] and the APR(APR) EOS (chapter 5.12 of [48], based on [44]). The latter uses a mixed phase to describe the transition to the pion condensate which therefore smooths the EOS. The fitting coefficients for the nucleonic GPPVA (DD2) EOS [41,49,50] are also provided. The data, as well as references and details for all EOSs are publicly available in tabulated form from the COMPOSE database [9]; the naming convention is the same as in this database, too.

Throughout the whole paper we use geometrized units where $c = 1$ and $G = 1$, except in Sec. II B.

The paper is organized as follows: Secs. II and III are dedicated to the description of procedures to represent one- and two-argument EOSs, respectively. Results are presented in Sec. IV with a comparison to static quantities (maximum mass, tidal deformability) and dynamic quantities (radial oscillation frequencies) both against published values and between the two fitting schemes. In particular a study of the influence of the choice of the crust is shown, as well as a comparison between frequencies of one- and two-argument EOSs. Conclusions are drawn in Sec. V.

II. REPRESENTATION OF ONE-ARGUMENT EOSs

This section is devoted to the presentation of the fitting schemes to parametrize barotropic EOSs that describe cold neutron stars in β equilibrium. Two schemes are presented and for each one, the global strategy is the following: the fitting scheme is applied to the core of the NS, i.e., for densities above some threshold $n_{\mathrm{lim},2}$; for densities below $n_{\mathrm{lim},1}$ a polytrope is considered for the crust. In between, a GPP is used to get a continuous matching of thermodynamic quantities: energy density e, pressure p, and sound speed c_s, both at $n_{\mathrm{lim},1}$ and $n_{\mathrm{lim},2}$.

A. Pseudopolytropes

We start with a fitting functional that we call *pseudopolytropes*. If $\varepsilon = e/m_B n_B - 1$ is the rescaled internal energy per particle (excluding rest-mass energy), with n_B the baryon number density, m_B the baryon mass, and e the total energy density, then the basic functional is

$$\varepsilon(n_B) = g(n_B) n_B^{\alpha}, \tag{1}$$

where g is an arbitrary function. The name pseudopolytrope is justified by the following: the choice of $g = \kappa/m_B\alpha$, where κ is a constant and denoting $\gamma = \alpha + 1$ yields a polytrope

$$p = n_B^2 \left(\frac{\partial \varepsilon}{\partial n_B}\right)_{T,Y_e} = n_B^2 \frac{\mathrm{d}\varepsilon}{\mathrm{d}n_B} = \kappa n_B^{\gamma}, \tag{2}$$

where p is the pressure. In order to account for an arbitrary crust, following the approach by [24], we add two parameters L and d such that the final functional is

$$\varepsilon(n_B) = g(n_B) n_B^{\alpha} + d - \frac{L}{n_B}. \tag{3}$$

The fitting coefficients will be α and the coefficients $\{\bar{a}_i\}_{i \in [\![0,n]\!]}$ of g, which we choose to be a polynomial:

$$g(x = \ln(n_B\ [\mathrm{fm}^{-3}])) = \sum_{i=0}^{n} \bar{a}_i x^i. \tag{4}$$

Their values will be adjusted by fitting the functional and its derivatives, whereas most parametrizations use only a single thermodynamic quantity to perform the fits.

From now on, x denotes the natural logarithm of the density n_B expressed in fm^{-3}. In order to perform a $\mathcal{C}^2$ stitching of the fit and an arbitrary crust, i.e., with continuous sound speed, we add a single intermediate density interval that is described by GPP formalism:

$$e_{\mathrm{GPP}}(n_B) = \frac{K_{\mathrm{GPP}}}{\Gamma_{\mathrm{GPP}} - 1} n_B^{\Gamma_{\mathrm{GPP}}} + (1 + d_{\mathrm{GPP}}) n_B - L_{\mathrm{GPP}}, \tag{5}$$

$$p_{\mathrm{GPP}}(n_B) = K_{\mathrm{GPP}} n_B^{\Gamma_{\mathrm{GPP}}} + L_{\mathrm{GPP}}. \tag{6}$$

Then, for a given crust defined by pressure and energy density profiles $p_c(n_B), e_c(n_B)$, there are three junction conditions at two densities $n_{\mathrm{lim},i}$, $i = 1$, 2, with $n_{\mathrm{lim},1} < n_{\mathrm{lim},2}$ that allow us to determine the six parameters $K_{\mathrm{GPP}}, \Gamma_{\mathrm{GPP}}, d_{\mathrm{GPP}}, L_{\mathrm{GPP}}, d, L$:

$$K_{\mathrm{GPP}} \Gamma_{\mathrm{GPP}} n_{\mathrm{lim},1}^{\Gamma_{\mathrm{GPP}}-1} = \frac{\mathrm{d}p_c}{\mathrm{d}n_B}(n_{\mathrm{lim},1}), \tag{7}$$

$$K_{\mathrm{GPP}} \Gamma_{\mathrm{GPP}} n_{\mathrm{lim},2}^{\Gamma_{\mathrm{GPP}}} = n_{\mathrm{lim},2} \left(\frac{\mathrm{d}(g(x)e^{\alpha x})}{\mathrm{d}x}(n_{\mathrm{lim},2}) + \frac{\mathrm{d}^2(g(x)e^{\alpha x})}{\mathrm{d}x^2}(n_{\mathrm{lim},2}) \right), \tag{8}$$

$$K_{\mathrm{GPP}} n_{\mathrm{lim},1}^{\Gamma_{\mathrm{GPP}}} + L_{\mathrm{GPP}} = p_c(n_{\mathrm{lim},1}), \tag{9}$$

$$K_{\mathrm{GPP}} n_{\mathrm{lim},2}^{\Gamma_{\mathrm{GPP}}} + L_{\mathrm{GPP}} = n_{\mathrm{lim},2} \frac{\mathrm{d}(g(x)e^{\alpha x})}{\mathrm{d}x}(n_{\mathrm{lim},2}) + L, \tag{10}$$

$$\frac{K_{\mathrm{GPP}}}{\Gamma_{\mathrm{GPP}} - 1} n_{\mathrm{lim},1}^{\Gamma_{\mathrm{GPP}}} + (1 + d_{\mathrm{GPP}}) n_{\mathrm{lim},1} - L_{\mathrm{GPP}} = e_c(n_{\mathrm{lim},1}), \tag{11}$$

$$\frac{K_{\mathrm{GPP}}}{\Gamma_{\mathrm{GPP}} - 1} n_{\mathrm{lim},2}^{\Gamma_{\mathrm{GPP}}-1} + d_{\mathrm{GPP}} - \frac{L_{\mathrm{GPP}}}{n_{\mathrm{lim},2}} = g(x_{\mathrm{lim},2}) e^{\alpha x_{\mathrm{lim},2}} + d - \frac{L}{n_{\mathrm{lim},2}}. \tag{12}$$

They correspond, by groups of two, to the continuity conditions of the internal energy and its first two derivatives. The first two equations are independent of $d_{\mathrm{GPP}}, L_{\mathrm{GPP}}, d, L$ and are solved with the non-linear vector function root-finder ROOT of the SCIPY.OPTIMIZE PYTHON library [51] to determine K_{GPP} and L_{GPP}. Only those first two equations are coupled, while the subsequent four equations can be solved successively to directly determine $L_{\mathrm{GPP}}, L, d_{\mathrm{GPP}}, d$ in this order. The fit is performed with a minimization of the following cost function:

$$E(\{\bar{a}_j\}, \alpha, d, L) = \frac{1}{x_{\max} - x_{\min}} \sum_X \sum_i \left(\frac{X_{\mathrm{tab},i} - X_{\mathrm{fit}}(x_i, \{\bar{a}_j\}, \alpha, d, L)}{X_{\mathrm{tab},i}} \right)^2 \Delta x_i, \tag{13}$$

where $x_{\max,\min}$ are the limiting densities of the chosen fitting interval, Δx_i is the log-density step of the table, i.e., if the densities of the table are discretized as $\{x_i, i \in [0, N]\}$ where $x_0 = x_{\min} \leq x_1 \leq \ldots \leq x_{N-1} \leq x_N = x_{\max}$, then $\Delta x_i = x_{i+1} - x_i$ when $i = 0, \ldots, N-1$, and $\Delta x_N = \Delta x_{N-1}$ and the variable X spans the chosen quantities to fit on, making the procedure a joint fit. For the one-argument fits the fit is performed on ε/n_B, $\ln(p/n_B)$, and Γ_1 [defined by Eq. (A12)], which are chosen to represent the internal energy ε and its first two derivatives, rescaled so that they are all of close order of magnitude.

We start by producing a set of fit coefficients with $d = L = 0$, thanks to a linear least-square fit of ε with respect to x performed with the CURVE_FIT routine of SCIPY.OPTIMIZE [51]. This educated guess is then used as the starting point of the minimization of Eq. (13). At every step of the procedure, $K_{\mathrm{GPP}}, \Gamma_{\mathrm{GPP}}, d_{\mathrm{GPP}}, L_{\mathrm{GPP}}, d, L$ can be computed from the current value of the coefficients. In practice, the crust is taken to be a polytrope for which the parameters (κ, γ) are chosen freely:

$$p_c(n_B) = \kappa n_B^{\gamma}. \tag{14}$$

Once γ is chosen, a fine-tuning of κ is done by hand to ensure that the maximal mass of the EOS is recovered. The results of the fit are reported in Table I for one-argument fits

TABLE I. One-argument EOS fit coefficients for the pseudopolytrope scheme.

	$\bar{a}_1$	$\bar{a}_2$	$\bar{a}_3$	$\bar{a}_4$	$\bar{a}_5$	$\bar{a}_6$	$\bar{a}_7$	α
RG(SLy4) [38,46,47]	0.28803	0.094928	0.0078768	−0.013071	0.0010821	−0.0010058	-6.6725×10^{-8}	1.5444
APR(APR) [44,48]	0.31909	0.12187	0.026877	−0.042652	0.016685	0.014534	0.0044882	1.9044
GPPVA(DD2) [41,49,50]	0.49196	−0.029608	−0.16060	0.090142	0.15724	0.053312	0.0062917	1.6799

of RG(SLy4) [38,46,47], APR(APR) [44,48] and GPPVA (DD2) [41,49,50].

B. The Potekhin-Pearson fitting scheme

References [31,32] present an analytical representation between the log of the pressure, $\log_{10} p \equiv \zeta$, and the log of the total energy density, $\log_{10}(\hat{e}[\mathrm{g \cdot cm^{-3}}]) \equiv \xi$ according to

$$\zeta = K + \frac{a_1 + a_2\xi + a_3\xi^3}{1 + a_4\xi} f_0(a_5(\xi - a_6)) + (a_7 + a_8\xi) \times f_0(a_9(a_6 - \xi)) + (a_{10} + a_{11}\xi) f_0(a_{12}(a_{13} - \xi)) + (a_{14} + a_{15}\xi) f_0(a_{16}(a_{17} - \xi)) + \frac{a_{18}}{1 + [a_{20}(\xi - a_{19})]^2} + \frac{a_{21}}{1 + [a_{23}(\xi - a_{22})]^2}, \tag{15}$$

where $f_0(x) = \{\exp(x) + 1\}^{-1}$, a_i are the fitting coefficients, and $\hat{e} = e/c^2$ is in $\mathrm{g\,cm^{-3}}$. Setting $K = 0$ gives the pressure in units of $\mathrm{dyn\,cm^{-2}}$, while $K = -33.2047$ gives the pressure in $\mathrm{MeV\,fm^{-3}}$.

Reference [32] showed that Eq. (15) could calculate the pressure with typical errors of about one per cent for the Brussels-Montreal Skyrme functionals, for densities in the range $6 \lesssim \xi \lesssim 16$. Indeed, each of the terms in Eq. (15) address a specific region of the NS (see Fig. 1); the first term is associated with the outer crust while the second, third and fourth terms describe the inner crust and the core regions. The fifth and sixth terms describe the neutron drip and the core-crust boundary, respectively.

Despite the fact that Eq. (15) can compute the pressure over the whole NS domain, we neglect the terms associated with the crust since our aim is to model the high-density part of the EOSs only. We therefore apply the analytical fit

$$\zeta = K + (a_2 + a_3\xi) f_0(a_4(a_1 - \xi)) + (a_5 + a_6\xi) f_0(a_7(a_8 - \xi)) + (a_9 + a_{10}\xi) f_0(a_{11}(a_{12} - \xi)) + \frac{a_{13}}{1 + [a_{15}(\xi - a_{14})]^2} \tag{16}$$

to the CompOSE tabulated values of pressure and total energy densities where $n_\mathrm{B} \geq 0.05\ \mathrm{fm^{-3}}$. This lower limit in n_B for the fitting window was chosen by hand to ensure good quality fits. In accordance with the GPP approach the pressure is then computed with

$$p(e) = 10^{\zeta(\xi)} + L. \tag{17}$$

The crust model is then added as described in Sec. II A. The equations describing the continuity of the pressure gradient, the pressure and the energy density at the boundary $n_{\mathrm{lim},2}$ for the Potekhin-Pearson scheme are, respectively,

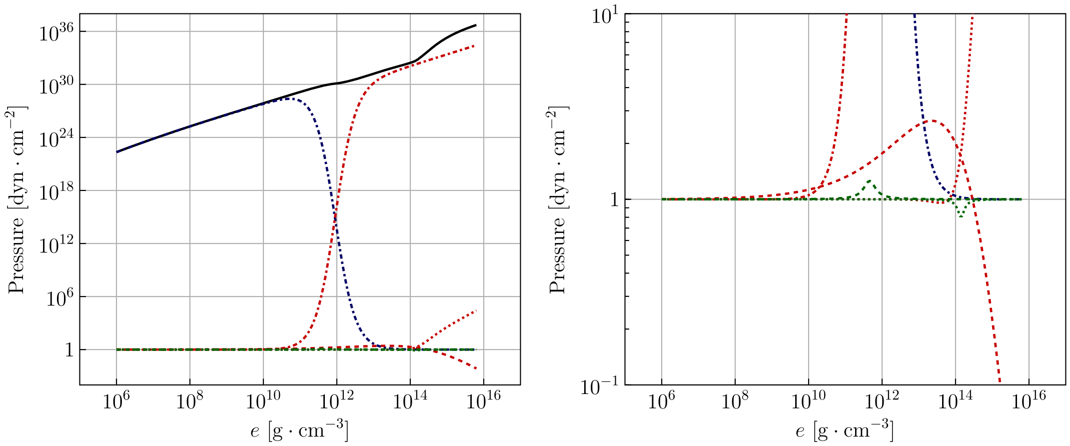

FIG. 1. Contribution of each of the terms in Eq. (15) to the total fit (solid, black curve) for the Brussels-Montreal Skyrme 24 equation of state, using the fit coefficients presented in [32]. The right panel is an enlargement of the lower part of the left panel. Term 1: blue, dot-dashed; term 2: red, dot-dashed; term 3: red, dotted; term 4: red, dashed; term 5: green, dashed, term 6: green, dotted.

TABLE II. Fit parameters for one-argument EOSs. κ is expressed in the set of geometrized units supplemented with $M_\odot = 1$.

	$n_{\mathrm{lim},1}$ [fm^{-3}]	$n_{\mathrm{lim},2}$ [fm^{-3}]	κ [geom]	γ
RG(SLy4) [38,46,47]	10^{-4}	10^{-2}	0.140	1.34
APR(APR) [44,48]	10^{-4}	10^{-2}	0.178	1.34
GPPVA(DD2) [41,49,50]	10^{-5}	8×10^{-2}	0.0140	1.34

$$K_{\mathrm{GPP}}\Gamma_{\mathrm{GPP}} n_{\mathrm{lim},2}^{\Gamma_{\mathrm{GPP}}-1} = \frac{\mathrm{d}p(n_{\mathrm{lim},2})}{\mathrm{d}n_{\mathrm{B}}} = \frac{p(e_{\mathrm{lim},2})+e_{\mathrm{lim},2}}{n_{\mathrm{lim},2}}\frac{p(e_{\mathrm{lim},2})}{e_{\mathrm{lim},2}}\frac{\mathrm{d}\zeta}{\mathrm{d}\xi}, \tag{18}$$

$$K_{\mathrm{GPP}} n_{\mathrm{lim},2}^{\Gamma_{\mathrm{GPP}}} + L_{\mathrm{GPP}} = p(e_{\mathrm{lim},2}) + L, \tag{19}$$

$$\frac{K_{\mathrm{GPP}}}{\Gamma_{\mathrm{GPP}}-1} n_{\mathrm{lim},2}^{\Gamma_{\mathrm{GPP}}} + (1+d_{\mathrm{GPP}})n_{\mathrm{lim},2} - L_{\mathrm{GPP}} = e_{\mathrm{lim},2} + (1+d)n_{\mathrm{lim},2} - L. \tag{20}$$

Here, $\mathrm{d}\zeta/\mathrm{d}\xi$ is calculated from Eq. (16) using the SYMPY library for symbolic computation, $e_{\mathrm{lim},2}$ is the total energy density at $n_{\mathrm{lim},2}$ and $p(e_{\mathrm{lim},2})$ is the pressure at this location, again calculated with Eq. (16). The value of e for a given n_{B} is calculated by inverting

$$\ln\left(\frac{n_{\mathrm{B}}}{n_0}\right) = \int_{e_0}^{e} \frac{\mathrm{d}e'}{p(e')+e'}, \tag{21}$$

[see Eq. (3) of [52]] where e_0 is the first data point in the fitting interval for the total energy density, and n_0 is the initial baryon density which, in turn, is calculated from the definition of the enthalpy

$$n_0 = \frac{e_0 + p(e_0)}{h_0}, \tag{22}$$

where h_0 is the first data point in the fitting interval for the enthalpy per baryon, and is calculated from the tables provided for a given EOS using the COMPOSE software, and $p(e_0)$ is calculated from the fit. We use the values of κ, γ and $n_{\mathrm{lim},1}$ for the crust model presented in Sec. II A (cf. Table II). However, we fine-tuned the values of $n_{\mathrm{lim},2}$ to ensure good quality fits. We use 0.04, 0.03, and 0.04 fm^{-3} for the barotropic RG(SLy4) [38,46,47], APR (APR) [44,48], and GPPVA(DD2) [41,49,50], respectively. For the two-argument equations of state RG(SLy4) [38,39], SRO(APR) [42,43], and HS(DD2) [40,41] we use 0.07, 0.05, and 0.04 fm^{-3}, respectively. The results of the fit for the barotropic RG(SLy4) [38,46,47], APR(APR) [44,48] and GPPVA(DD2) [41,49,50] are given in Table III.

TABLE III. One-argument EOS fit coefficients for the Potekhin-Pearson scheme.

a_i	RG(SLy4) [38,46,47]	APR(APR) [44,48]	GPPVA(DD2) [41,49,50]
a_1	12.28260	12.01420	11.18370
a_2	13.86452	13.84209	15.72280
a_3	1.37955	1.31315	1.02836
a_4	3.50552	3.58798	3.62161
a_5	−30.75774	−30.71754	−28.57321
a_6	2.10272	2.20118	2.08129
a_7	3.70203	3.45345	5.16074
a_8	13.87372	14.58988	14.44345
a_9	30.13271	30.15473	31.78975
a_{10}	−2.03900	−2.03509	−1.99041
a_{11}	1.57077	1.91274	1.62725
a_{12}	15.28327	14.77801	13.7790
a_{13}	0.013287	0.023175	0.16426
a_{14}	14.30128	14.46573	14.27033
a_{15}	9.076260	9.09854	3.45961

III. REPRESENTATION OF TWO-ARGUMENT EOSs

For the purposes of cold EOSs that describe matter out of the weak β equilibrium, we shall consider general purpose tables from COMPOSE that are described with the three arguments (n_B, Y_e, T) and, as an approximation, use the first temperature entry of the table, which in general corresponds to a temperature $T \lesssim 100$ keV. The thermal effects at this temperature are relevant only in the outer part of the outer crust. This part of the EOS is not captured by the fits, therefore we consider that the first temperature entry of the table is an excellent approximation to the zero-temperature case.

We will adapt the procedure described in the previous section for the two-argument form of the tables. In addition to imposing pressure and sound speed continuity, we also ensure the existence of β equilibrium for all densities. The neutrinoless β-equilibrium condition is

$$\mu_{l_e} = 0, \tag{23}$$

where μ_{l_e} is the chemical potential of leptons. Using the definition $\mu_{l_e} = (\frac{\partial\varepsilon}{\partial n_e})_{n_B}$ (see Sec. 3.7 of [33]), it can be rewritten as

$$\left(\frac{\partial\varepsilon}{\partial Y_e}\right)_{n_B} = 0, \tag{24}$$

implying that $\forall n_B$, ε must have a minimum in the Y_e direction. Because the original EOS should also possess a β equilibrium, this condition should automatically be fulfilled in the high-density part, provided that the fit is accurate enough. However, as the low-density part consists of a generic polytropic crust, special care should be brought when constructing it for EOSs with two arguments.

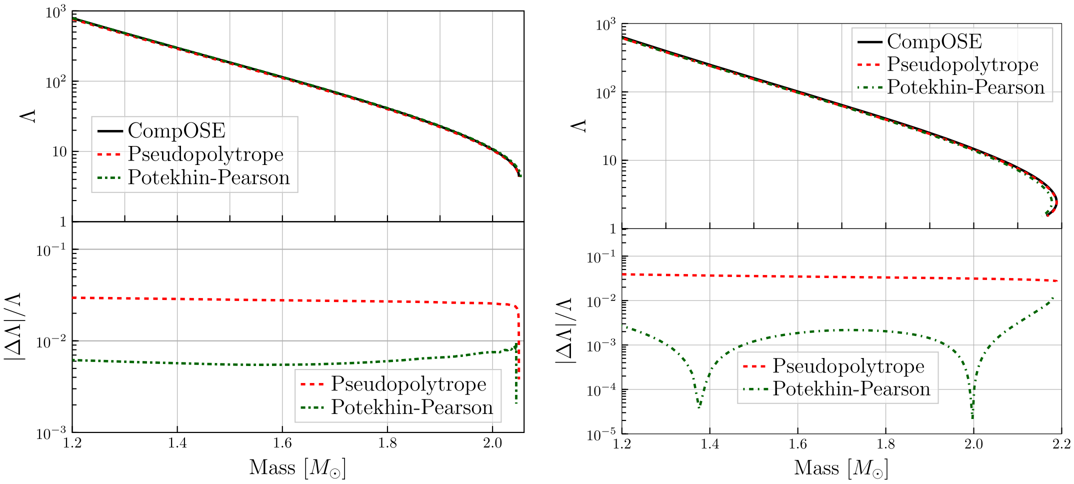

(a) RG(SLy4) [38, 46, 47].

(b) APR(APR) [44, 48].

FIG. 2. Mass-deformability diagrams of the two cold EOSs. The bottom panel is the relative difference of the fits with respect to the original COMPOSE EOS. The relative differences have been computed at constant fraction of the maximum mass: $\Lambda_{\mathrm{EOS}}(M_1)$ was compared to $\Lambda_{\mathrm{fit}}(M_2)$, where M_2 is defined by $M_2/M_{\mathrm{fit,max}} = M_1/M_{\mathrm{EOS,max}}$.

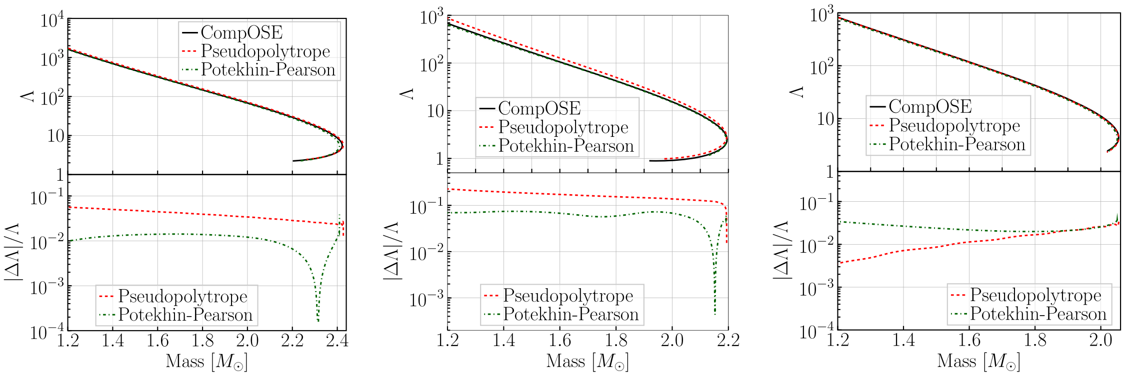

(a) HS(DD2) [40, 41].

(b) SRO(APR) [42, 43].

(c) RG(SLy4) [38, 39].

FIG. 3. Mass-deformability diagrams of the β-equilibrated versions of the three general purpose EOSs. The bottom panel is the relative difference of the fits with respect to the original COMPOSE EOS. The relative differences have been computed at constant fraction of the maximum mass: $\Lambda_{\mathrm{EOS}}(M_1)$ was compared to $\Lambda_{\mathrm{fit}}(M_2)$ where M_2 is defined by $M_2/M_{\mathrm{fit,max}} = M_1/M_{\mathrm{EOS,max}}$.

The procedure is the following: according to the frozen composition principle, the two-argument EOS is considered as a collection of N_Y one-argument EOSs, N_Y being the number of tabulated values of Y_e, each of which is fitted according to the procedure described in Sec. II, meaning that we once again have three parts: a high-density part where the fit is performed, a low-density part where a simplified polytropic model is applied, and an intermediate part described with a single-piece GPP to connect the two other parts. This time, for the pseudopolytrope we choose to perform the fit on $X = \{\varepsilon/n_B\}$ only, to help reduce parameter dispersion from one slice to the next. For the Potekhin-Pearson scheme, we perform a fit of the pressure only. Each new fit is initialized with the optimal coefficients of the previous one.

For each fit, the outermost polytrope has γ fixed and κ taken to be a polynomial in Y_e:

$$\kappa(Y_e) = \sum_{i=0}^{n_\kappa} \kappa_i Y_e^i. \tag{25}$$

We determine the coefficients κ_i as a polynomial fit to $\varepsilon(Y_e, n_{\mathrm{lim},2})$, i.e., we write $\forall i \in [\![0, n_\kappa]\!], \kappa_i = A\kappa_i'$ and determine the $\{\kappa_i'\}_{i\in[\![0,n_\kappa]\!]}$ with the fit. Then the constant A is chosen freely. This procedure guarantees that there is always a β-equilibrium solution in the low-density part. Only the intermediate part is left, where GPP expressions are used to connect the crust to the fit. They are built to provide pressure and sound speed continuity at the junctions, but there is no simple theoretical argument that

TABLE IV. Comparison with existing parametrizations of barotropic EOSs. Data from other parametrizations have been collected from tables available within the articles. $M_{\rm max}$ is the maximum mass of the EOS in units of $M_\odot$, and $\Lambda_{1.4}$ is the value of the tidal deformability of a $1.4 M_\odot$ NS. The value provided in [24] for the maximum mass of APR is $2.057 M_\odot$, but we recomputed it using their coefficients and found the value tabulated here.

	RG(SLy4)		APR(APR)		GPPVA(DD2)	
Parametrization	$M_{\rm max}$	$\Lambda_{1.4}$	$M_{\rm max}$	$\Lambda_{1.4}$	$M_{\rm max}$	$\Lambda_{1.4}$
Original EOS	2.050	297.0	2.188	249.1	2.418	676.8
Pseudopolytrope (this work)	2.050	289.5	2.188	240.2	2.418	696.4
Potekhin-Pearson fit (this work)	2.041	289.1	2.178	240.3	2.417	683.9
Piecewise polytropes [22]	2.049	✗	2.213	✗	✗	✗
GPP [24]	2.053	310.6	2.168*	255.0	✗	✗
Suleiman *et al.* [23]	2.049	304.98	✗	✗	2.417	697.9

ensures the existence of a β equilibrium in the intermediate part. However, we find that, at the cost of fine-tuning the parameter A by hand, this is always the case. The result of the fitting procedure is a collection of N_Y coefficient lists. For example with the pseudopolytrope, using seven coefficients in Eq. (4) gives 16 fitting coefficients per slice: $8 + 2$ for the high-density region and six that are deduced in the mid-density region to ensure that the matching conditions are fulfilled. In the end, the formalism is semianalytic because to compute the thermodynamics at a nontabulated value of Y_e, one must interpolate between two neighbor fit expressions. Moreover, producing initial data requires the computation of the β-equilibrated EOS, which is entirely numerical. For example, the β-equilibrated EOS yielded by a two-argument pseudopolytrope is not a one-argument pseudopolytrope, but is rather a curve in the (n_B, Y_e) plane. It is important to note that the procedure makes no assumption regarding the fitting scheme, which means that in principle it can be applied to any fit of the high density part of a given EOS.

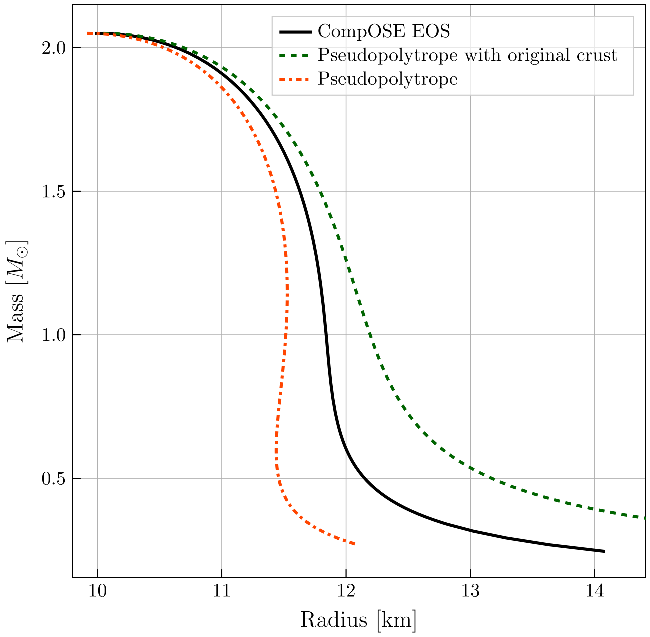

FIG. 4. Influence of the crust on the radius. The solid line is the COMPOSE EOS. The dashed line is a pseudopolytropic fit, and the dash-dotted line is the same fit but where the crust has been replaced with the one of the original barotropic RG(SLy4) [38,46,47] table.

IV. RESULTS

In this section all tests are run with isolated, spherically symmetric, nonrotating NSs using the code described in [33]. The fits are tested on the EOSs described in the introduction.

A. Static quantities

In order to check our fits' performances we first check the static quantities: mass M, radius R, tidal deformability Λ. The definition of the tidal deformability is the following [53,54]:

$$\Lambda = \frac{2}{3}\Xi^{-5}k_2, \tag{26}$$

where $\Xi = M/R$ is the compactness parameter and k_2 the so-called $\ell = 2$ tidal Love number [53]. These quantities can be obtained from an $\ell = 2$ linear perturbation of a spherically symmetric star equilibrium obtained from the Tolmann-Oppenheimer-Volkoff equations [53,55]. To compare the static quantities, we compute the mass-deformability diagrams of the fitted EOS and we compare them with the curves obtained with the original table. The results are shown on Figs. 2(a) and 2(b) for the one-argument fits, and Figs. 3(a)–3(c) for the two-argument fits. The fits capture well the deformability: regarding the one-argument EOSs the error on the computation of Λ is 3% for RG(SLy4) [38,46,47] and 4% for APR(APR) [44,48] with the pseudopolytrope, and the Potekhin-Pearson fit reproduces the values of Λ with an error that never exceeds 1%. The fits perform well for two-argument EOSs as the error is also of the order of a few percent, except for the SRO(APR)

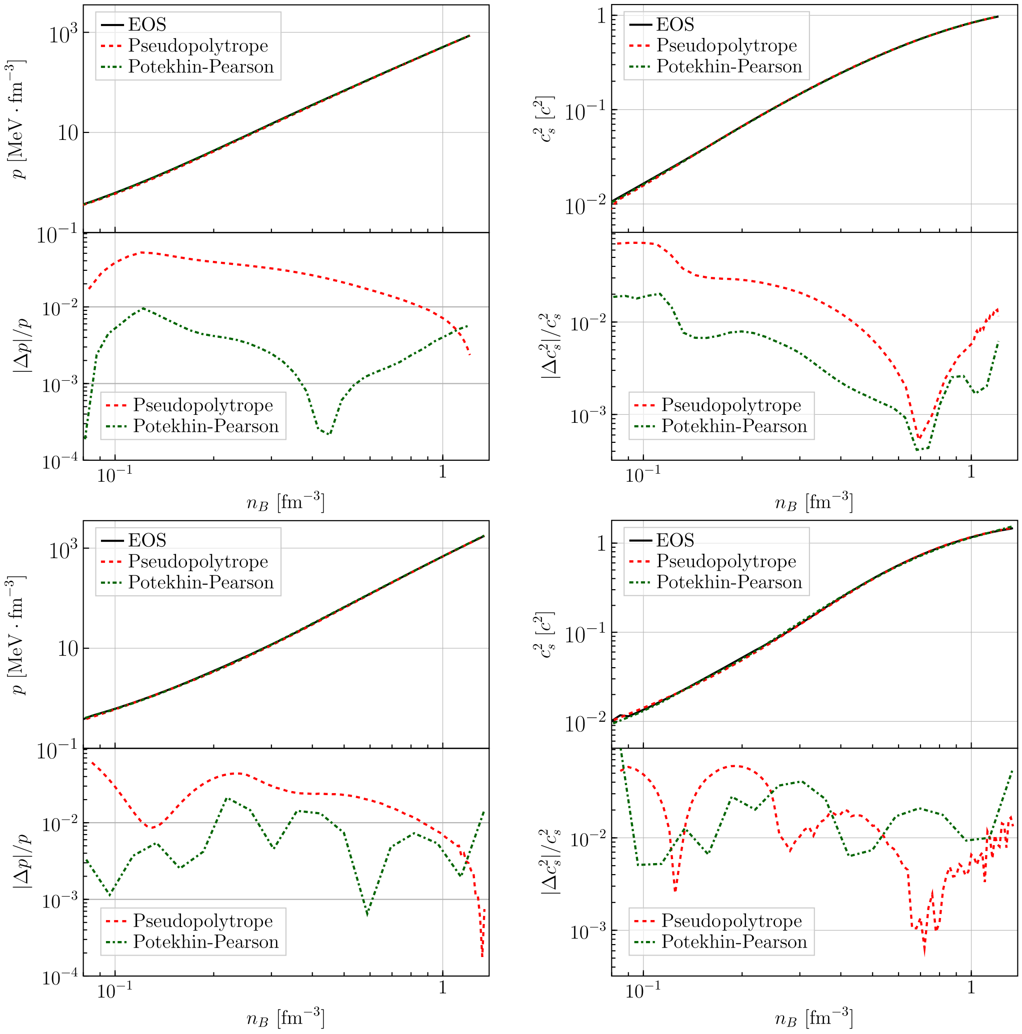

(a) Pressure vs baryon number density. (b) Sound speed vs baryon number density.

FIG. 5. Thermodynamical profiles of two barotropic EOSs: RG(SLy4) [38,46,47] (top), APR(APR) [44,48] (bottom).

EOS [42,43] for which the phase transition to a pion condensate around $n_B = 0.2\ \mathrm{fm}^{-3}$ is treated with a Maxwell type construction, which is not well reproduced by our fits, and where the error of the pseudopolytrope exceeds 10%. The Potekhin-Pearson approach does slightly better but the error remains close to 10% as again the phase transition region is not well reproduced. For SRO(APR) we point out that the minimization procedure to add the crust, as described in Sec. II A, fails to converge for the Potekhin-Pearson scheme if we use $n_{\mathrm{lim},2} = 0.2\ \mathrm{fm}^{-3}$ as applied by the pseudopolytrope formalism. To remove the phase transition associated with the pions, we instead replace the tabulated values of the adiabatic index, $\Gamma = \mathrm{d}\log p/\mathrm{d}\log e$ in the vicinity of the phase transition with smoothed values using linear interpolation. The pressure is then recomputed from these updated values of the adiabtic index. Note that the one-argument APR(APR) EOS considers a mixed phase at the transition to the pion-condensed phase which smooths the EOS and that it can thus be much better reproduced by our fits.

These figures also show that the maximum masses for each of the EOSs considered are well reproduced (see Table IV). On the other hand, we know that the predicted radius strongly depends on how the crust-core transition is made, as well as the actual crust model [56,57]; the error can reach one kilometer for a $1M_\odot$ neutron star. We emphasize that changing the matching between the crust and the core may induce this error even without changing the physics. The drastic effect of the crust on the radius is shown in Fig. 4, where the mass radius diagrams of the barotropic RG(SLy4) EOS [38,46,47] is compared with the pseudopolytropic fit, as well as the fit where the EOS crust was replaced with the one of the original EOS. For a canonical $1.40M_\odot$ neutron star, we compare the radii and deformabilities with stars constructed with the RG(SLy4) EOS and its fits: (i) the original table, (ii) the pseudopolytropic fit, and (iii) the pseudopolytropic fit where the crust

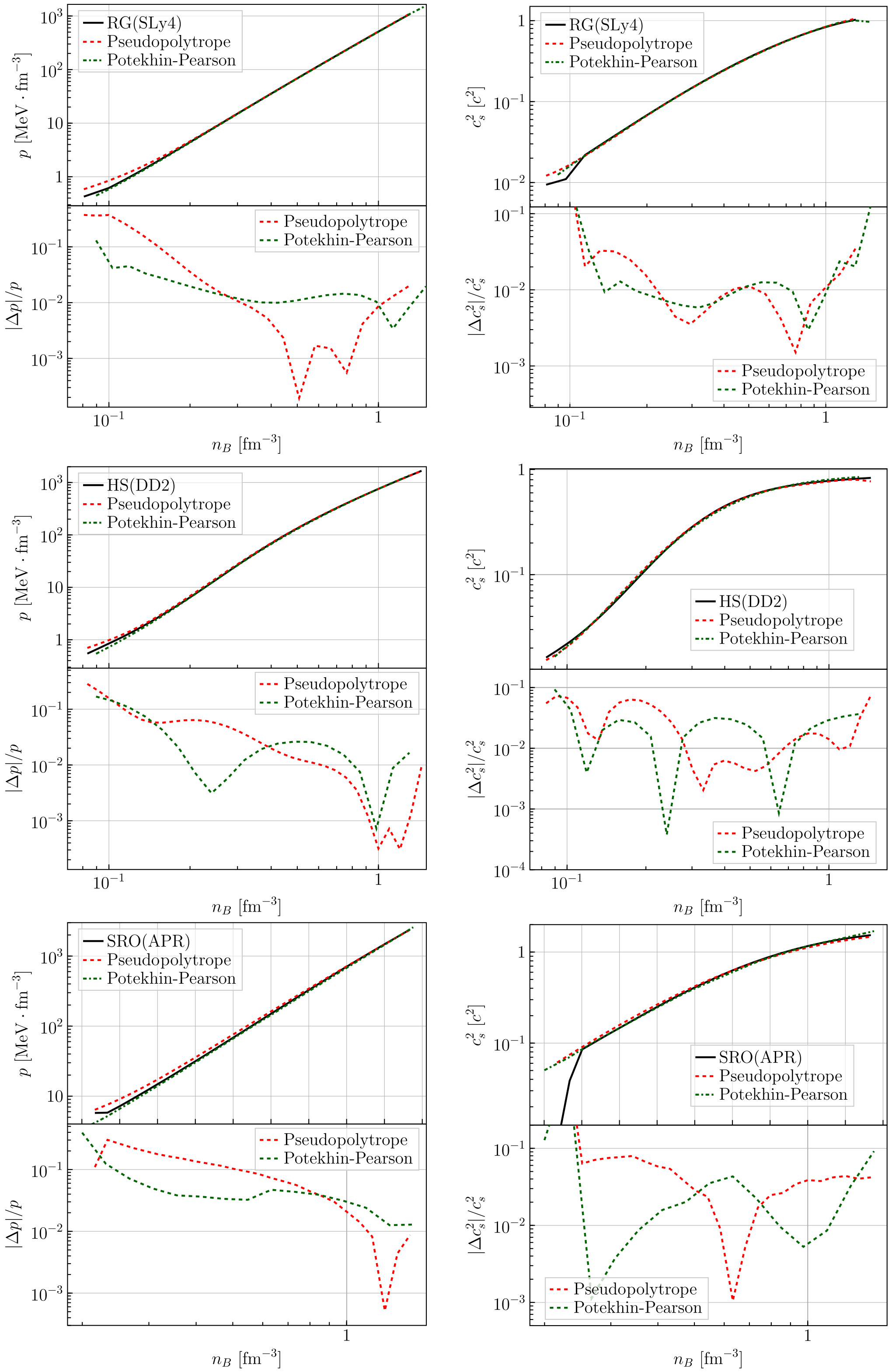

(a) Pressure vs baryon number density.

(b) Sound speed vs baryon number density.

FIG. 6. Two-argument fits: comparison between the β-equilibrated versions of the original tables and the β-equilibrated versions of the fits.

has been replaced with the one of the original table. We give the values for RG(SLy4):

(i) $R = 11.7$ km and $\Lambda = 297$
(ii) $R = 11.5$ km and $\Lambda = 290$
(iii) $R = 11.9$ km and $\Lambda = 290$

and APR(APR):

(i) $R = 11.3$ km and $\Lambda = 249$
(ii) $R = 11.2$ km and $\Lambda = 240$
(iii) $R = 11.2$ km and $\Lambda = 231$.

Replacing the crust has changed the value of the radius and the deformability by a few percents while Fig. 9 shows that the frequencies remain unchanged when varying the crust model. The pressure and sound speed profiles are represented in Fig. 5 for the one-argument EOSs and Fig. 6 for the β-equilibrated version of the two-argument EOSs. All in all the fits show a good agreement compared to the original EOS, especially when no phase transition is present, as the relative difference in the thermodynamic quantities between the fit and the original EOS remains below 10%, except close to $n_{\mathrm{lim},2}$ where the low-density matching procedure tends to mildly degrade the quality of the fit. The phase transition of SRO(APR) [42,43] can be seen in Fig. 6: the sudden drop of the sound speed is due to a discontinuity in the pressure derivative.

B. Dynamic quantities

We also compare the frequencies yielded by using the fits in our code that was presented and benchmarked in [33] with those tabulated in the literature. The frequency extraction procedure is a maximum search in the spectrum coupled with a quadratic interpolation of the closest neighbors. As shown on Fig. 7, our frequencies are in good agreement with the ones tabulated in [4,58], where a perturbative approach is used. Although Barta [58] has developed a dissipative formalism in the perturbative framework, his approach was benchmarked on the EOSs of [4] and the EOSs that are used in those two papers are the same versions of APR and SLy4 chosen here. The error of the fits on the sound speed profile is comparable with the error between the approaches of [4,58], we therefore consider the values of frequencies to be compatible with one another. Figure 8 shows the mass-frequency diagram for the RG(SLy4) EOS [38,46,47]. Even though in Ref. [58] frequency values for the fundamental mode of oscillating spherically symmetric NS are presented for this particular EOS, those frequencies do not vanish as the mass approaches the maximum mass of the EOS. This suggests that there was an issue in the computation of the frequencies and we therefore do not include them in the figure. For both $f(M)$ diagrams the frequency of the fundamental mode approaches zero towards the maximum mass as expected. It is also notable that the Potekhin-Pearson approach and the pseudopolytrope give very close frequencies one to another. Considering that the Potekhin-Pearson approach uses 15 fit coefficients per slice while the pseudopolytropic approach uses only 3 to 7 fit coefficients per slice, the latter shows its efficiency in reproducing dynamical NS oscillation modes compared to the former.

The influence of the crust on the frequencies is shown in Fig. 9: a pseudopolytropic fit is performed for three different values of the polytropic index in the crust and the $f(M)$ diagram computed for the three fits. The x axis of the plot is the mass rescaled to the maximum mass yielded by the fit to aid comparison. The frequencies are almost unchanged between the three fits, which is in contrast with the influence the choice of the crust has on the radius. It shows the limited influence of the crust dynamics on the oscillation modes of a NS. A possible explanation for this is that we do not actually take the detailed physics of the crust into account in the hydrodynamic simulations as the whole star is modeled by a perfect fluid, and an accurate description of the crust would correspond to use models of the crystalline structure. Also at this stage the hydrodynamical code does

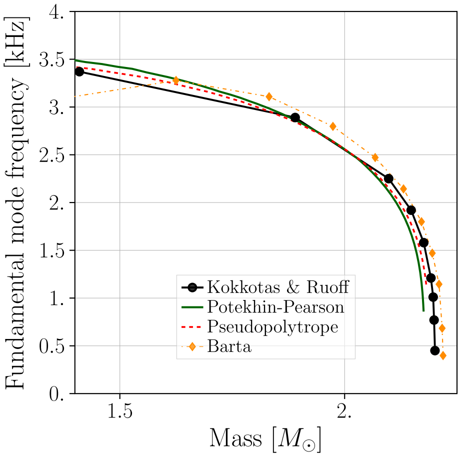

FIG. 7. $f(M)$ diagram for barotropic APR(APR) [44,48] EOS compared with values taken from Table A.17 of [4] and Table 2 of [58].

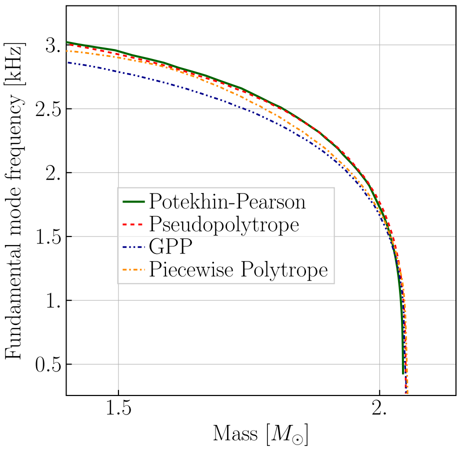

FIG. 8. $f(M)$ diagram for barotropic RG(SLy4) [38,46,47] EOS. The data for the GPPs and piecewise polytropes have been digitized from [24] with ENGAUGE-DIGITIZER [59].

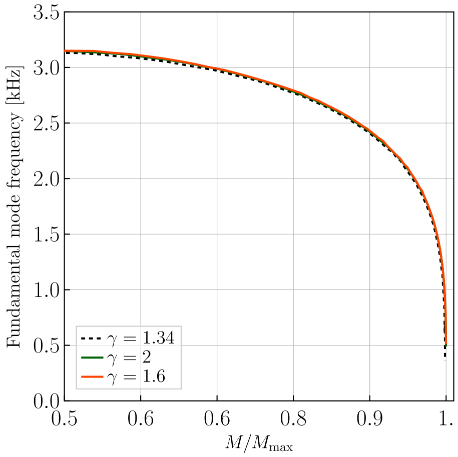

FIG. 9. $f(M)$ diagram for three pseudopolytropic fits with three different choices of polytropic index in the crust.

not support the nonmonotonic behavior of the sound speed in the crust of [60].

The $f(M)$ curves for the two-argument fits of the three chosen general purpose EOSs are plotted on Fig. 10. The frequencies agree quite well between the two fitting procedures, and it is also notable that going from the β-equilibrated version of the EOS to the two-argument version gives very similar frequencies. We note that, at low neutron star masses, the Potekhin-Pearson scheme predicts higher fundamental frequencies than the pseudopolytrope formalism. This could be a consequence of the impact that the different values of $n_{\mathrm{lim},2}$ used by the two fitting schemes has on the properties of the intermediate region that connects the polytropic crust with the fitted core. Therefore, for SRO(APR), the intermediate region may have a non-negligible impact on the fundamental frequencies. Unlike the EOSs considered in Fig. 11, the $f(M)$ curves for the β-equilibrated and two-argument versions of SRO(APR) do not match. This could be a consequence of the crude smoothing used to remove the pion condensate. The fundamental difference between the two simulations is the production of neutrinos, which is here taken into account through the evolution equation for Y_e. This is a simple advection equation with a source term, see Appendix B. The source terms σ are computed from the expressions in [37], and depend strongly on the temperature, namely being proportional to $(T/10^9\ \mathrm{K})^5$ for direct Urca processes and $(T/10^9\ \mathrm{K})^7$ for modified Urca processes. Because we choose the first entries of the tables that typically correspond to a temperature of 100 keV, the actual computation of source terms gives values so small that they are below the machine accuracy and therefore are virtually zero. Therefore the simulations happen exactly as if no neutrinos were emitted. The initial data used to perform the evolution are computed with the β-equilibrated version of the fits and then the star numerically exits the β-equilibrium state thanks to the fact that $\mu_{l_e} \neq 0$ numerically.

Comparing the results of the one- and two-argument fits for RG(SLy4) [38,46,47] shows that the frequencies converge for higher masses, cf. Figs. 11 and 12. The small discrepancy for higher mass is due to the slightly different value of maximum mass between the β-equilibrated version of the two-argument fit of HS(DD2) [40,41] and the one-argument fit of GPPVA(DD2) [41,49,50]. This is consistent with the previous paragraph. We recall that the tables are slightly different: the one-argument versions on COMPOSE exactly correspond to zero temperature, whereas the general purpose tables we used for two-argument fits start at a low but nonzero temperature. The latter also rely on more general calculations that do not consider a crystalline structure in the low-density inhomogeneous phase. However, as the study of the influence of the crust on the frequencies of the fundamental mode suggests, these differences that mainly concern the crust should have very little effect on the values of the frequencies. Also, the direct comparison cannot be made for APR, because even though [42] uses the same nuclear interaction as [44], the final EOS is different: the one-argument version was computed with a mixed phase whereas the general purpose one was computed with two distinct phases, yielding a first order

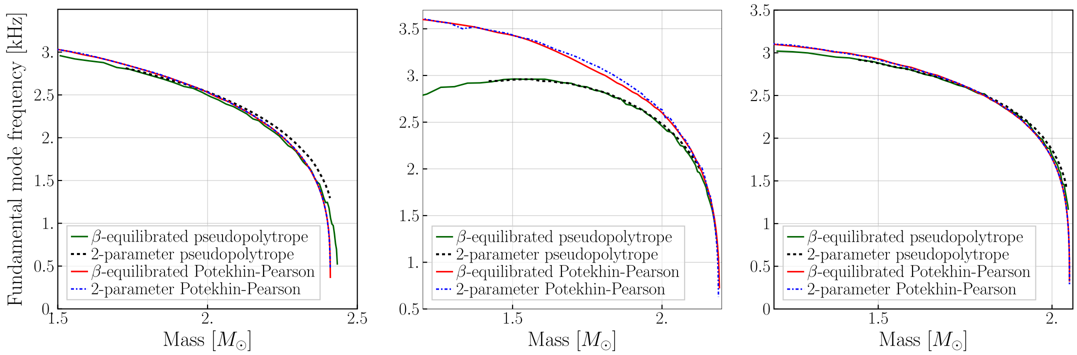

(a) HS(DD2) [40, 41]. (b) SRO(APR) [42, 43]. (c) RG(SLy4) [38, 39].

FIG. 10. $f(M)$ diagram for the three general purpose EOSs.

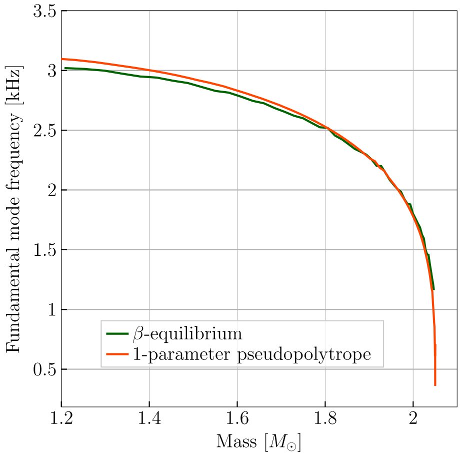

FIG. 11. Comparison of fundamental mode frequency between the one-argument pseudopolytropic fit of barotropic RG(SLy4) [38,46,47] and the β-equilibrated version of the two-argument pseudopolytropic fit of RG(SLy4) [38,39].

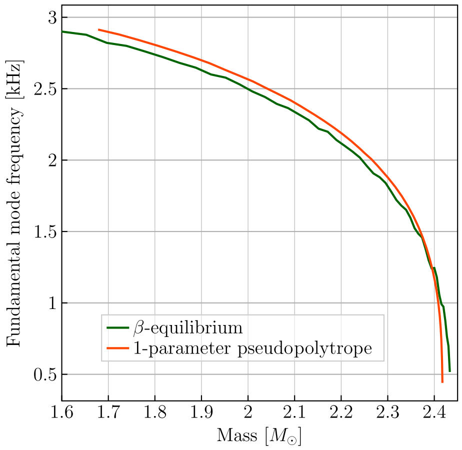

FIG. 12. Comparison of fundamental mode frequency between the one-argument pseudopolytropic fit of barotropic GPPVA (DD2) [41,49,50] and the β-equilibrated version of the two-argument pseudopolytropic fit of HS(DD2) [40,41].

transition. Overall, the differences are most certainly due to the increased number of fit coefficients for the two-argument functional.

V. CONCLUSIONS

We presented two systematic ways to represent any given EOS by an analytic fit function. The low-density (crust) part of the EOSs is not represented by the fits and we consider simplified expressions for this part. In principle, we could match a widely used crust, for instance the one from [60], or attach a consistent crust obtained e.g., from the CUTER tool [61]. This tool, based on the work of [62], allows us to attach a physically accurate crust to any EOS. The hydrodynamical code that we use, however, does not support the nonmonotonic behavior of the sound speed that happens around the transition from the inner to the outer crust at $n_B \approx 2 \times 10^{-4}$ fm^{-3}. This is also the reason why we drop the crust terms in the Potekhin-Pearson model. These issues might be related to the nonconvex hydrodynamics triggered by such behaviors, in connection with the so-called fundamental derivative [63,64]. Our simplfied approach can be justified by the fact that the detailed crust physics is not the most important when looking at NS oscillations.

A first asset of the approach lies in its economical nature: instead of storing a large table, any EOS can be represented in the form of a few coefficients and a formula, as an be expected from a parametrization. For example, the general purpose tables used in the paper have a total of 826 708 [RG(SLy4) [38,39]], 1 239 300 [HS(DD2) [40,41]] and 3 151 302 [SRO(APR) [42,43]] thermodynamic entries (the files' sizes are respectively 70, 167, and 496 MB. The number of data entries reduce to 6 667, 15 300, and 23 694, respectively, when considering only the lowest temperature entry). On the other hand fitting with the Potekhin-Pearson model gives 15 coefficients per slice which corresponds to around 900 coefficients, and the pseudopolytrope gives 3 to 7 coefficients per slice, depending on the choice of the degree of the polynomial g, which amounts to 200 to 500 coefficients. A second asset is the low-density stitching procedure: considering an analytic low-density model, it gives continuous sound speed profiles even down to zero densities, which is important for dynamical simulations of neutron stars, and the procedure is in principle applicable to any EOS parametrization. Finally, we have demonstrated that the approach made the fitting of two-argument EOSs possible thanks to the simplified crust model, from which we were then able to compute macroscopic static quantities as well as to perform dynamical simulations from which frequencies could be extracted. The Potekhin-Pearson model allowed us to compare our novel approach with an already existing fitting scheme that is known for its precision in the thermodynamical profiles. The pseudopolytrope does almost as well as the Potekhin-Pearson approach in reproducing the macroscopic static quantities of the original EOS, except in the presence of a phase transition where the thermodynamics is harder to capture, but where both approaches fail to reproduce it faithfully. However the fundamental radial frequencies of one-argument EOSs are well reproduced by both approaches, and compatible when independently applied to two-argument EOSs. In that regard, the pseudopolytrope might be preferable as the number of fitting coefficients is reduced compared to the Potekhin-Pearson approach. We provided, whenever possible, a comparison between the published values of macroscopic static quantities and radial oscillation frequencies obtained with previous EOS parametrizations. We also have shown that changing the crust has a very limited effect on the values of the oscillation frequencies of neutron stars, especially for stars with a high mass where the crust is thinner. We recall here that we do not use a detailed description of the crust in the hydrodynamical simulations and further work in that direction would be needed to assess the extent of this result. Extensions of the work would be improving the two-argument fitting scheme by making it fully analytical, and extending it to three-argument EOS tables with temperature as an additional argument. We give a few words on EOSs that include hyperons: we tried to apply the fits on one of those EOSs. Both fitting procedures were unable to successfully capture the phase transition at high densities which induces a discontinuity in the sound speed. Since the discontinuity is physical, one way to address this would be to consider several zones with different fitting functionals. This would be worth exploring for future versions of the fits. We plan to make the pseudopolytrope fitting code publicly available as a tool of COMPOSE in the future.

The codes used in this study are still in development and have not been published yet. The data that support the findings of this study are available upon reasonable request from the authors.

ACKNOWLEDGMENTS

G. S. would like to thank Michael O'Boyle for his useful insight on the generalized piecewise polytropes and Dániel Barta for details on his paper on radial oscillations of neutron stars. G. S., P. J. D., J. N., and M. O. acknowledge financial support from the Agence Nationale de la Recherche (ANR) under Contract No. ANR-22-CE31-0001-01 and from the CNRS International Research Project (IRP) "Origine des éléments lourds dans l'univers: Astres Compacts et Nucléosynthèse (ACNu)." J. A. P. acknowledges the support through the Grant No. PID2021-127495NB-I00 funded by MCIN/AEI/10.13039/501100011033 and by the European Union, the Astrophysics and High Energy Physics programme of the Generalitat Valenciana ASFAE/2022/026 funded by MCIN and the European Union NextGenerationEU (PRTR-C17.I1) and the Prometeo excellence programme Grant No. CIPROM/2022/13. The authors gratefully acknowledge the Italian Instituto Nazionale de Fisica Nucleare (INFN), the French Centre National de la Recherche Scientifique (CNRS) and the Netherlands Organization for Scientific Research for the construction and operation of the Virgo detector and the creation and support of the EGO consortium. The authors thank the anonymous referee for thoughtful comments that helped improve the quality of the manuscript.

APPENDIX A: ANALYTICAL FORMULAS OF PSEUDOPOLYTROPIC THERMODYNAMICS

The internal energy ε serves as a potential from which all other thermodynamic quantities can be derived, and we here compile the expressions of the most common ones, expressed as a function of ε and its derivatives or as the fitting coefficients of the expression (1) and $x = \ln(n_B\ [\mathrm{fm}^{-3}])$:

$$\varepsilon(x) = e^{\alpha x}\sum_{k=0}^{n}\bar{a}_k x^k + d - e^{-x}L, \tag{A1}$$

$$\frac{\mathrm{d}\varepsilon}{\mathrm{d}x}(x) = e^{\alpha x}\left[\alpha\sum_{k=0}^{n}\bar{a}_k x^k + \sum_{k=1}^{n}k\bar{a}_k x^{k-1}\right] + e^{-x}L, \tag{A2}$$

$$\frac{\mathrm{d}^2\varepsilon}{\mathrm{d}x^2}(x) = e^{\alpha x}\left[\alpha^2\sum_{k=0}^{n}\bar{a}_k x^k + 2\alpha\sum_{k=1}^{n}k\bar{a}_k x^{k-1} + \sum_{k=2}^{n}k(k-1)\bar{a}_k x^{k-2}\right] - e^{-x}L, \tag{A3}$$

$$\frac{p}{m_B} = e^{x}\frac{\mathrm{d}\varepsilon}{\mathrm{d}x}, \tag{A4}$$

$$= e^{(\alpha+1)x}\left[\alpha\sum_{k=0}^{n}\bar{a}_k x^k + \sum_{k=1}^{n}k\bar{a}_k x^{k-1}\right] + L, \tag{A5}$$

$$\frac{e}{m_B} = e^{x}(\varepsilon + 1), \tag{A6}$$

$$= e^{(\alpha+1)x}\sum_{k=0}^{n}\bar{a}_k x^k + e^{x}(1+d) - L, \tag{A7}$$

$$H = \ln\left(\frac{e+p}{m_B n_B}\right) = \ln\left(1 + \varepsilon + \frac{\mathrm{d}\varepsilon}{\mathrm{d}x}\right), \tag{A8}$$

$$= \ln\left(1 + d + e^{\alpha x}\left((\alpha+1)\sum_{k=0}^{n}\bar{a}_k x^k + \sum_{k=1}^{n}k\bar{a}_k x^{k-1}\right)\right), \tag{A9}$$

$$c_s^2 = \frac{\mathrm{d}p}{\mathrm{d}e} = \frac{\frac{\mathrm{d}\varepsilon}{\mathrm{d}x} + \frac{\mathrm{d}^2\varepsilon}{\mathrm{d}x^2}}{1 + \varepsilon + \frac{\mathrm{d}\varepsilon}{\mathrm{d}x}}, \tag{A10}$$

$$= \frac{e^{\alpha x}[\alpha(\alpha+1)\sum_{k=0}^{n}\bar{a}_k x^k + (2\alpha+1)\sum_{k=1}^{n}k\bar{a}_k x^{k-1} + \sum_{k=2}^{n}k(k-1)\bar{a}_k x^{k-2}]}{1 + d + e^{\alpha x}[(\alpha+1)\sum_{k=0}^{n}\bar{a}_k x^k + \sum_{k=1}^{n}k\bar{a}_k x^k]}, \tag{A11}$$

$$\Gamma_1 = \frac{\mathrm{d}\ln p}{\mathrm{d}x} = 1 + \frac{\frac{\mathrm{d}^2\varepsilon}{\mathrm{d}x^2}}{\frac{\mathrm{d}\varepsilon}{\mathrm{d}x}}, \tag{A12}$$

$$= \frac{e^{\alpha x}[\alpha(\alpha+1)\sum_{k=0}^{n}\bar{a}_k x^k + (2\alpha+1)\sum_{k=1}^{n}k\bar{a}_k x^{k-1} + \sum_{k=2}^{n}k(k-1)\bar{a}_k x^{k-2}]}{e^{\alpha x}[\alpha\sum_{k=0}^{n}\bar{a}_k x^k + \sum_{k=1}^{n}k\bar{a}_k x^{k-1}] + e^{-x}L}. \tag{A13}$$

APPENDIX B: EVOLUTION EQUATION FOR THE ELECTRON FRACTION

Under the 3 + 1 decomposition of general relativity, if γ_{ij} denotes the induced three-metric on spacelike hypersurfaces to which we associate D_i its corresponding covariant derivative, N the lapse function, β^i the shift vector, U^i the Eulerian velocity, $\Gamma = (1 - U_i U^i)^{-1/2}$ the Lorentz factor, and we denote by $v^i = NU^i - \beta^i$ the coordinate velocity, then the evolution equation of Y_e the electron fraction is

$$\partial_t Y_e + v^i D_i Y_e = \frac{N}{\Gamma}\frac{\sigma}{n_B}. \tag{B1}$$

The details on the derivation of this equation can be found in [33].

---

[1] M. Oertel, M. Hempel, T. Klähn, and S. Typel, Rev. Mod. Phys. **89**, 015007 (2017).

[2] F. Banyuls, J. A. Font, J. M. Ibanez, J. M. Marti, and J. A. Miralles, Astrophys. J. **476**, 221 (1997).

[3] M. Shibata and K. ō. Uryū, Phys. Rev. D **61**, 064001 (2000).

[4] K. D. Kokkotas and J. Ruoff, Astron. Astrophys. **366**, 565 (2001).

[5] J. A. Font, T. Goodale, S. Iyer, M. Miller, L. Rezzolla, E. Seidel, N. Stergioulas, W.-M. Suen, and M. Tobias, Phys. Rev. D **65**, 084024 (2002).

[6] I. Cordero-Carrión, P. Cerdá-Durán, H. Dimmelmeier, J. L. Jaramillo, J. Novak, and E. Gourgoulhon, Phys. Rev. D **79**, 024017 (2009).

[7] F. Hébert, L. E. Kidder, and S. A. Teukolsky, Phys. Rev. D **98**, 044041 (2018).

[8] S. Rosswog and P. Diener, Classical Quantum Gravity **38**, 115002 (2021).

[9] S. Typel, M. Oertel, and T. Klähn, Phys. Part. Nucl. **46**, 633 (2015).

[10] M. Shibata, K. Taniguchi, and K. Uryū, Phys. Rev. D **71**, 084021 (2005).

[11] K. Hotokezaka, K. Kyutoku, H. Okawa, M. Shibata, and K. Kiuchi, Phys. Rev. D **83**, 124008 (2011).

[12] D. Radice, A. Perego, K. Hotokezaka, S. A. Fromm, S. Bernuzzi, and L. F. Roberts, Astrophys. J. **869**, 130 (2018).

[13] F. Zappa, S. Bernuzzi, D. Radice, and A. Perego, Mon. Not. R. Astron. Soc. **520**, 1481 (2023).

[14] B. Müller, H.-T. Janka, and H. Dimmelmeier, Astrophys. J. Suppl. Ser. **189**, 104 (2010).

[15] M. Hempel, T. Fischer, J. Schaffner-Bielich, and M. Liebendörfer, Astrophys. J. **748**, 70 (2012).

[16] O. Just, R. Bollig, H. T. Janka, M. Obergaulinger, R. Glas, and S. Nagataki, Mon. Not. R. Astron. Soc. **481**, 4786 (2018).

[17] T. Kuroda, T. Fischer, T. Takiwaki, and K. Kotake, Astrophys. J. **924**, 38 (2022).

[18] A. Pascal, J. Novak, and M. Oertel, Mon. Not. R. Astron. Soc. **511**, 356 (2022).

[19] M. V. Beznogov, J. Novak, D. Page, and A. R. Raduta, Astrophys. J. **942**, 72 (2023).

[20] K. Kiuchi, A. Reboul-Salze, M. Shibata, and Y. Sekiguchi, Nat. Astron. **8**, 298 (2024).

[21] F. D. Swesty, J. Comput. Phys. **127**, 118 (1996).

[22] J. S. Read, B. D. Lackey, B. J. Owen, and J. L. Friedman, Phys. Rev. D **79**, 124032 (2009).

[23] L. Suleiman, M. Fortin, J. L. Zdunik, and C. m. c. Providência, Phys. Rev. C **106**, 035805 (2022).

[24] M. F. O'Boyle, C. Markakis, N. Stergioulas, and J. S. Read, Phys. Rev. D **102**, 083027 (2020).

[25] L. Lindblom, Phys. Rev. D **82**, 103011 (2010).

[26] L. Lindblom, Phys. Rev. D **97**, 123019 (2018).

[27] L. Lindblom, Phys. Rev. D **105**, 063031 (2022).

[28] S. K. Greif, G. Raaijmakers, K. Hebeler, A. Schwenk, and A. L. Watts, Mon. Not. R. Astron. Soc. **485**, 5363 (2019).

[29] I. Legred, Y. Kim, N. Deppe, K. Chatziioannou, F. Foucart, F. m. c. Hébert, and L. E. Kidder, Phys. Rev. D **107**, 123017 (2023).

[30] C. A. Raithel, F. Özel, and D. Psaltis, Astrophys. J. **875**, 12 (2019).

[31] A. Y. Potekhin, A. F. Fantina, N. Chamel, J. M. Pearson, and S. Goriely, Astron. Astrophys. **560**, A48 (2013).

[32] J. M. Pearson, N. Chamel, A. Y. Potekhin, A. F. Fantina, C. Ducoin, A. K. Dutta, and S. Goriely, Mon. Not. R. Astron. Soc. **481**, 2994 (2018).

[33] G. Servignat, J. Novak, and I. Cordero-Carrión, Classical Quantum Gravity **40**, 105002 (2023).

[34] T. Celora, I. Hawke, P. C. Hammond, N. Andersson, and G. L. Comer, Phys. Rev. D **105**, 103016 (2022).

[35] G. Camelio, L. Gavassino, M. Antonelli, S. Bernuzzi, and B. Haskell, Phys. Rev. D **107**, 103031 (2023).

[36] G. Camelio, L. Gavassino, M. Antonelli, S. Bernuzzi, and B. Haskell, Phys. Rev. D **107**, 103032 (2023).

[37] P. Haensel, Astron. Astrophys. **262**, 131 (1992).

[38] F. Gulminelli and A. R. Raduta, Phys. Rev. C **92**, 055803 (2015).

[39] A. R. Raduta and F. Gulminelli, Nucl. Phys. **A983**, 252 (2019).

[40] M. Hempel and J. Schaffner-Bielich, Nucl. Phys. **A837**, 210 (2010).

[41] S. Typel, G. Röpke, T. Klähn, D. Blaschke, and H. H. Wolter, Phys. Rev. C **81**, 015803 (2010).

[42] A. S. Schneider, L. F. Roberts, and C. D. Ott, Phys. Rev. C **96**, 065802 (2017).

[43] A. S. Schneider, C. Constantinou, B. Muccioli, and M. Prakash, Phys. Rev. C **100**, 025803 (2019).

[44] A. Akmal, V. R. Pandharipande, and D. G. Ravenhall, Phys. Rev. C **58**, 1804 (1998).

[45] A. Akmal and V. Pandharipande, Phys. Rev. C **56**, 2261 (1997).

[46] E. Chabanat, P. Bonche, P. Haensel, J. Meyer, and R. Schaeffer, Nucl. Phys. **A635**, 231 (1998).

[47] P. Danielewicz and J. Lee, Nucl. Phys. **A818**, 36 (2009).

[48] *Neutron Stars 1, Vol. 326 of Astrophysics and Space Science Library*, edited by P. Haensel, A. Y. Potekhin, D. G. Yakovlev, F. Bertola, J. Cassinelli, C. Cesarsky, P. Ehrenfreund, O. Engvold, A. Heck, E. van den Heuvel *et al.* (Springer, New York, New York, NY, 2007), ISBN 978-0-387-33543-8 978-0-387-47301-7.

[49] F. Grill, H. Pais, C. Providência, I. Vidaña, and S. S. Avancini, Phys. Rev. C **90**, 045803 (2014).

[50] J. M. Pearson, N. Chamel, A. Y. Potekhin, A. F. Fantina, C. Ducoin, A. K. Dutta, and S. Goriely, Mon. Not. R. Astron. Soc. **481**, 2994 (2018).

[51] P. Virtanen, R. Gommers, T. E. Oliphant, M. Haberland, T. Reddy, D. Cournapeau, E. Burovski, P. Peterson, W. Weckesser, J. Bright *et al.*, Nat. Methods **17**, 261 (2020).

[52] P. Haensel and A. Y. Potekhin, Astron. Astrophys. **428**, 191 (2004).

[53] T. Hinderer, Astrophys. J. **677**, 1216 (2008).

[54] T. Malik, N. Alam, M. Fortin, C. Providência, B. K. Agrawal, T. K. Jha, B. Kumar, and S. K. Patra, Phys. Rev. C **98**, 035804 (2018).

[55] T. Hinderer, B. D. Lackey, R. N. Lang, and J. S. Read, Phys. Rev. D **81**, 123016 (2010).

[56] M. Fortin, C. Providência, A. R. Raduta, F. Gulminelli, J. L. Zdunik, P. Haensel, and M. Bejger, Phys. Rev. C **94**, 035804 (2016).

[57] L. Suleiman, M. Fortin, J. L. Zdunik, and P. Haensel, Phys. Rev. C **104**, 015801 (2021).

[58] D. Barta, Classical Quantum Gravity **38**, 185002 (2021).

[59] B. M. Mark Mitchell and E. D. S. Tobias Winchen *et al.*, Engauge digitizer software (2020), 10.5281/zenodo.3941227.

[60] F. Douchin and P. Haensel, Astron. Astrophys. **380**, 151 (2001).

[61] P. J. Davis, H. Dinh Thi, A. F. Fantina, F. Gulminelli, M. Oertel, and L. Suleiman (to be published).

[62] T. Carreau, F. Gulminelli, and J. Margueron, Eur. Phys. J. A **55**, 188 (2019).

[63] J. M. Ibáñez, I. Cordero-Carrión, J. M. Martí, and J. A. Miralles, Classical Quantum Gravity **30**, 057002 (2013).

[64] J. M. Ibáñez, A. Marquina, S. Serna, and M. A. Aloy, Mon. Not. R. Astron. Soc. **476**, 1100 (2018).